water

MDPI

Article

Photocatalytic Degradation of Typical Fibrates by N and F Co-Doped TiO_2 Nanotube Arrays Under Simulated Sunlight Irradiation

Xiangyu Chen [1,*], Hao Zhong [1], Juanjuan Yao [2], Jingye Gan [2], Haibing Cong [1] and Tengyi Zhu [1]

[1] College of Environmental Science and Engineering, Yangzhou University, Yangzhou 225127, China; mz120231306@stu.yzu.edu.cn (H.Z.); hbcong@yzu.edu.cn (H.C.); tyzhu@yzu.edu.cn (T.Z.)
[2] Key Laboratory of the Three Gorges Reservoir Regions Eco-Environment, Ministry of Education, Chongqing University, Chongqing 400045, China; yaojuanjuan@cqu.edu.cn (J.Y.); 27002734@alu.cqu.edu.cn (J.G.)
* Correspondence: xiangyuchen@yzu.edu.cn

Abstract

Fibrate pharmaceuticals (fibrates), as a widespread class of emerging contaminants, pose potential risks to both ecological systems and human health. The photocatalytic system based on nitrogen (N) and fluorine (F) co-doped TiO_2 nanotube arrays (NF-TNAs) provides a renewable solution for fibrate pharmaceutical removal from water, powered by inexhaustible sunlight. In this study, the degradation of two typical fibrates, i.e., bezafibrate (BZF) and ciprofibrate (CPF), under simulated sunlight irradiation through NF-TNAs were investigated. The photocatalytic degradation of BZF/CPF was achieved through combined radical and non-radical oxidation processes, while the generation and reaction mechanisms of associated reactive oxygen species (ROS) were examined. Electron paramagnetic resonance detection and quenching tests confirmed the existence of h^+, •OH, $O_2^{\bullet-}$, and $^1O_2$, with $O_2^{\bullet-}$ playing the predominant role. The transformation products (TPs) of BZF/CPF were identified through high-resolution mass spectrometry analysis combined with quantum chemical calculations to elucidate the degradation pathways. The influence of co-existing ions and typical natural organic matters (NOM) on BZF/CPF degradation were also tested. Eventually, the ecological risk of BZF/CPF transformation products was assessed through quantitative structure–activity relationship (QSAR) modeling, and the results showed that the proposed photocatalytic system can largely alleviate fibrate toxicity.

Keywords: fibrate pharmaceuticals; TiO_2 nanotube arrays; photocatalysis; degradation pathways

check for updates

Academic Editor: Gongduan Fan

Received: 14 June 2025
Revised: 10 July 2025
Accepted: 24 July 2025
Published: 29 July 2025

Citation: Chen, X.; Zhong, H.; Yao, J.; Gan, J.; Cong, H.; Zhu, T. Photocatalytic Degradation of Typical Fibrates by N and F Co-Doped TiO_2 Nanotube Arrays Under Simulated Sunlight Irradiation. *Water* **2025**, *17*, 2261. https://doi.org/10.3390/w17152261

Copyright: © 2025 by the authors. Licensee MDPI, Basel, Switzerland. This article is an open access article distributed under the terms and conditions of the Creative Commons Attribution (CC BY) license (https://creativecommons.org/licenses/by/4.0/).

1. Introduction

Pharmaceutical contaminants, including lipid-regulating agents such as fibrate pharmaceutical compounds (fibrates), are increasingly detected in wastewater due to their widespread use and incomplete removal in conventional treatment processes [1]. Fibrates are a class of amphipathic carboxylic acids and drugs that act as agonists of peroxisome proliferator-activated receptor alpha. They are widely employed to regulate blood lipid concentrations on a global scale [2,3]. Owing to its high consumption and limited metabolic degradation in humans, fibrates are frequently detected in various water systems, including wastewater, surface water, groundwater, or even drinking water, and reached a concentration about ng/L to μg/L levels [4,5]. However, due to their stable chemical structure, fibrates persist even at trace concentrations in modern water and wastewater treatment

systems, posing potential aqueous environment and human health risks [6–8]. Therefore, more effective treatment technologies need to be developed for fibrate degradation and mineralization.

In recent decades, studies have emphasized the role of photocatalysis in treating such persistent pollutants [9], particularly through modified titanium dioxide (TiO_2) nanomaterials [10]. TiO_2-based photocatalysis is one of the most promising advanced oxidation processes (AOPs) due to its strong oxidative capacity and stability. It represents a simple and convenient way to utilize the optical energy [11–14]. The generation of reactive oxygen species (ROS) through TiO_2 photocatalysis is crucial for breaking down the refractory structure of fibrate molecules. Sayed reported that TiO_2/Ti film with enhanced (001) facets could be synthesized and applied to fibrates degradation under UV light [15]. Lambropoulou found low concentration of representative fibrates could be degraded efficiently by TiO_2 under sunlight within 200 min [16]. Nevertheless, its practical application under visible light remained limited due to two critical drawbacks, including a broad band gap (~3.2 eV) and inefficient photo-induced charge carrier mobility [17,18]. In contrast to conventional TiO_2, nitrogen (N) and fluorine (F) co-doped TiO_2 nanotube arrays (NF-TNAs) have attracted significant interest owing to their superior solar absorption, enhanced electron transport, and improved quantum confinement effects. This is because that in situ N and F doping could narrow the bandgap of original TiO_2, and more reactive sites could also be generated [19–21]. Additionally, either the lifetime of photogenerated carriers is increased or more photogenerated electrons (e^-) transfer into the TNA after N and F doping, leading to enhanced photochemical performance [22,23]. Unlike powdered TiO_2, NF-TNAs are immobilized on a substrate, making them easy to recover and reuse without secondary pollution, and photocatalysis with NF-TNAs provides a potential way to remove fibrates. However, there are few studies that focus on investigating the degradation of typical fibrates by sunlight-driven NF-TNAs and relevant photocatalysis mechanisms; also, the degradation pathways of typical fibrates during NF-TNAs photocatalysis still need further exploration. Moreover, recent studies have utilized quantum chemical calculations based on molecular orbital theory to help elucidate degradation mechanisms by forecasting reactive sites for different reactive oxidizing species (ROS). However, there is a scarcity of theoretical research focused on predicting reaction sites in the photodegradation of fibrates. Therefore, research needs to be conducted to fill this gap by systematically investigating the photocatalytic performance of NF-TNAs and mechanism for fibrate degradation.

Herein, we are motivated to study the degradation and transformation of typical fibrates by NF-TNAs through simulated sunlight photocatalysis (i.e., NF-TNAs/sum system) comprehensively. Two kinds of typical fibrate drugs, bezafibrate (BZF) and ciprofibrate (CPF), were selected as the target pollutants in this study. The contribution of various ROS during photocatalysis were investigated through using targeted quenching experiments. Additionally, LC-MS/MS analysis combined with frontier molecular orbital computations was employed to identify the transformation byproducts (TPs) and elucidate the degradation pathways of the selected fibrates. The toxicity of BZF/CPF and its TPs generated during photocatalysis were investigated. Moreover, the influence of various anions, natural organic matter (NOM), and other factors on BZF/CPF degradation were investigated to explore this system's potential for practical application.

2. Materials and Methods

2.1. Materials

Bezafibrate (BZF, 99.9%), ciprofibrate (CPF, 99.9%), acetonitrile (HPLC grade), *tert*-butanol (TBA), 2-propanol, glycerine, L-histidine, tiron (sodium 1, 2-dihydroxybenzene, 3–5-disulfonate), and Ethylenediaminetetra acetic acid disodium (EDTA·2Na) were pur-

chased from Aladdin (Shanghai, China). Ammonium chloride (NH4Cl), ammonium fluoride (NH4F), and titanium (Ti) foil (0.25 mm thick, 99.9%) were purchased from Sigma Aldrich (St. Louis County, MO, USA). Stock solutions of BZF and CPF were prepared at concentrations of 10 mg/L, respectively. Preparation of the synthetic wastewater involved successive addition of Cl−, PO3−4, CO32−/HCO3−, and humic acid (HA).

Analytical-grade or upper reagents were used throughout this study. The Master-S water purification system (Shanghai, China) provided ultrapure water (18.2 MΩ) for preparing all working and stock solutions, except where otherwise mentioned.

2.2. Synthesis and Characterization of the NF-TNAs

Preparation of the NF-TNAs photocatalytic material was carried out via anodization, as detailed in our previous work [24,25]. Specifically, a titanium foil was ultrasonically cleaned sequentially in ethanol, acetone, and deionized water before undergoing anodization. The anodizing electrolyte consisted of a glycerol and deionized water mixture (9:1 by volume) containing 0.25 M NH4Cl and 0.36 M NH4F. A two-electrode electrochemical setup (2.0 cm distance) was employed, with the Ti foil as the anode and a platinum foil as the cathode, applying a constant voltage of 20.0 V using a DC power supply. Following 1.0 h of anodization, the resulting sample was cleaned with deionized water, air-dried, and subsequently annealed at 500 °C for 1.0 h under a nitrogen environment. The samples morphology were observed by Thermo Fisher Quattro S field emission scanning electron microscopy (SEM). The X-ray diffraction (XRD) spectra were acquired via a SHIMADZU XRD-600 system (Kyoto, Japan) using Cu Kα radiation (λ = 0.1540 nm) at 40 kV and 30 mA. X-ray photoelectron spectroscopy (XPS) analysis was conducted using an ESCALAB250 photoelectron spectrometer (Waltham, MA, USA) equipped with a monochromatic Al Kα radiation source.

2.3. Fibrates Degradation Experiments

Two kinds of typical fibrates, i.e., bezafibrate (BZF) and ciprofibrate (CPF), were selected for the execution of this study. The drugs were selected based on the commercial availability of raw materials, structural representativeness, and evidence of few scientific studies regarding the drugs on the research subject. All experiments were carried out in a cuboid quartz reactor (5.0 cm × 4.0 cm × 6.0 cm); then, the NF-TNAs (3.0 × 4.0 cm), which was fixed by a holder, was vertically immersed in the reactor. The fibrate wastewater was at its natural pH (about 6.8) and no pH control was conducted during the entirety of the photocatalytic degradation experiments.

In each test, the quartz reactor was loaded with 100 mL of a pre-prepared solution of 1 mg/L BZF or CPF. To ensure optimal adsorption of BZF/CPF on the NF-TNAs, the suspension was magnetically agitated in the dark for half an hour before light irradiation. A 500 W xenon lamp (Institute of Electric Light Source, Beijing, China) served as the simulated sunlight source. The light intensity on the NF-TNAs surface was measured at 100 mW/cm^2 (λ > 290 nm) using an optical power meter (CEL-NP2000-1, Education Au-light Co., Beijing, China). Samples (approximately 2.5 mL) of the BZF/CPF solution were collected at predetermined intervals and filtered through a 0.22 μm membrane. All experiments were conducted under isothermal conditions (25.0 ± 1.0 °C) maintained using a water bath. Specific ROS participation in BZF/CPF degradation was probed using selective chemical quenchers. The quenching agents for •OH, h^+, $O_2^{\bullet-}$, and $^1O_2$ were tert-butanol (TBA), EDTA·2Na, tiron (sodium 1, 2-dihydroxybenzene, 3–5-disulfonate), and L-histidine, respectively [26,27]. Text S1 (Supplementary Material) details the determination of second-order rate constants for ROS quenchers and their optimal concentrations. All tests were conducted in triplicate, with reported values representing averaged results from

these repetitions. The photocatalytic degradation efficiency under various experimental conditions was assessed using a pseudo-first-order kinetic model (Equation (1)) [28].

$$\ln \frac{C}{C_0} = -k_{20}t \quad (1)$$

Here, C_0 and C refer to initial and time-dependent concentrations, respectively, while k_{20} is the pseudo-first-order rate constant calculated for the initial 20 min reaction period. Additionally, k_{120}, which denotes the rate constant during the whole 120 min degradation, was also calculated for contrast.

2.4. Analytical Methods

The concentrations of BZF and CPF were quantified using a Hitachi 5100 HPLC system (Tokyo, Japan)with UV detection at 230 nm. Transformation products (TPs) were analyzed by LC-MS/MS (Shimadzu LC 30A coupled with AB SCIEX Triple TOF 4600 (Kyoto, Japan)). Additional methodological details are provided in Text S2 of the Supplementary Materials.

Quantum chemical calculations employed the B3LYP functional with 6-31 + G(d) basis set and polarizable continuum solvent model within Gaussian 09 to determine frontier molecular orbitals of BZF and CPF [29]. Molecular orbital visualization was performed with GaussView 5.0, generating HOMO and LUMO isosurfaces for different protonation states of BZF and CPF in water. Using Multiwfn 3.6 with literature-based interpretation, we analyzed atomic orbital participation in HOMO/LUMO formation, subsequently identifying potential reactive centers for ROS interactions. [30]. Atomic numbering of BZF/CPF assigned in this study and the calculation results is presented in Figures S5 and S6, Supplementary Materials. Frontier orbital theory predicts that atoms with significant HOMO contributions are prone to electrophilic attacks (like •OH, $^1O_2$ and h^+) or hydrogen abstraction by $O_2^{\bullet -}$, while those with significant LUMO contributions favor nucleophilic reactions like $O_2^{\bullet -}$.

3. Results and Discussions

3.1. Characterization of NF-TNA

As presented in Figure 1a,b, the SEM micrographs of the NF-TNAs reveal well-aligned nanotube arrays on the titanium substrate. The well-organized tube structures exhibit uniform dimensions with average tube diameter of 150 nm and wall thickness of 15 nm. The XRD spectrum of the synthesized NF-TNAs is presented in Figure S1, Supplementary Materials. The diffraction peaks at 2θ = 25.3°, 48.2°, 55.2°, and 74.3° are found in the XRD pattern, confirming pure anatase-phase TiO_2 (JCPDS card No. 21:1272) in the NF-TNAs, with complete absence of rutile or brookite phase. This indicates that the synthesized NF-TNAs is pure anatase phase.

Figure 1c,d shows the XPS spectra in the N 1s and F 1s regions of the NF-TNAs, and the full XPS spectrum of the NF-TNAs sample was presented in Figure S2. Deconvolution of the N 1s spectrum (Figure 1c) reveals four distinct peaks at 396.3, 398.9, 400.1, and 401.3 eV. The peak at 396.3 eV represents the lowest binding energy, which corresponds to N atoms forming direct bonds with Ti. This indicates substitutional N at O lattice sites [31,32]. The peak at 398.9 eV corresponds to interstitial N atoms coordinated with lattice O [33]. Additionally, the higher binding energy signals at 400.1 and 401.3 eV originate from surface nitrogen species, primarily NO_x and NH_x [34]. The core-level spectrum of fluorine in Figure 1d can be deconvoluted into peaks around 684.3, 688.1, and 690.2 eV. The more intense peak at 684.3 eV has been attributed to F^- ions physically adsorbed on the TiO_2 surface [35]. The higher binding energy peaks at 688.1 and 690.2 eV correspond to fluorine substitution at oxygen sites within the TiO_2 [36].

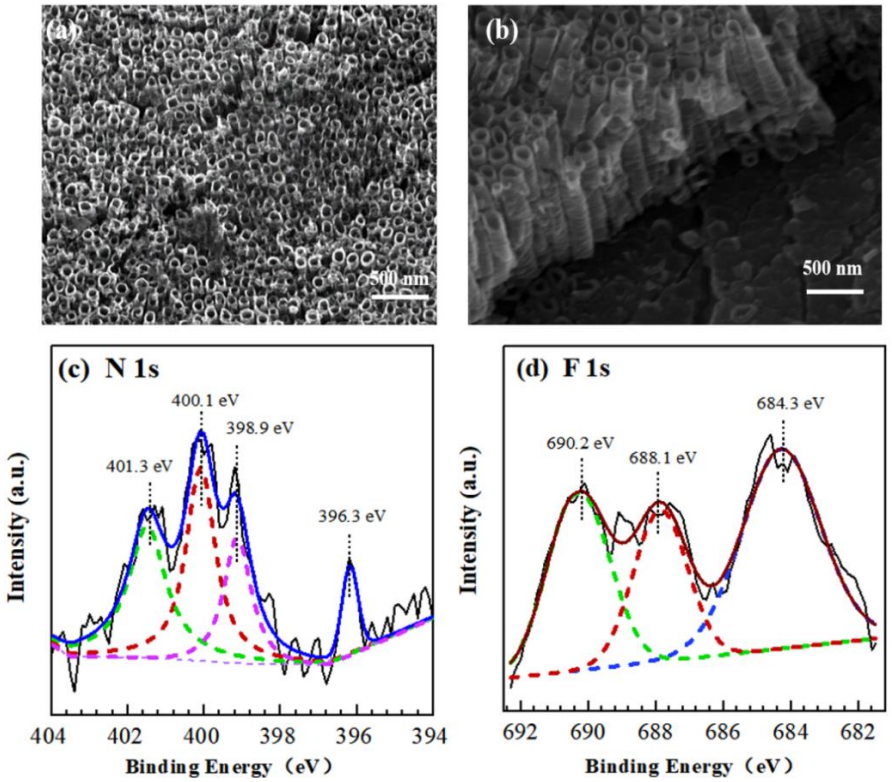


Figure 1. (**a**,**b**) SEM image of NF-TNAs, (**c**) XPS spectra of N 1s, (**d**) XPS spectra of F 1s.

3.2. Photocatalytic Performance of NF-TNA Toward BZF and CPF Degradation

The adsorption ability of the NF-TNAs in the dark and the degradation efficiency of BZF and CPF during photocatalysis through NF-TNAs are shown in Figure 2. There was no obvious loss of BZF and CPF molecules that could be detected during dark-controlled adsorption experiments or direct photolysis, indicating negligible degradation by hydrolysis, thermal degradation, and photolysis. This is mainly due to the chemical stability of fibrates. Additionally, the UV-Vis absorption spectrum of these two kinds of fibrate are shown in Figure S2. It is obvious that the maximum absorption peak of BZF and CPF are found to be located at 228 and 233 nm, indicating that they can hardly be removed by simulated sunlight illumination (>300 nm).

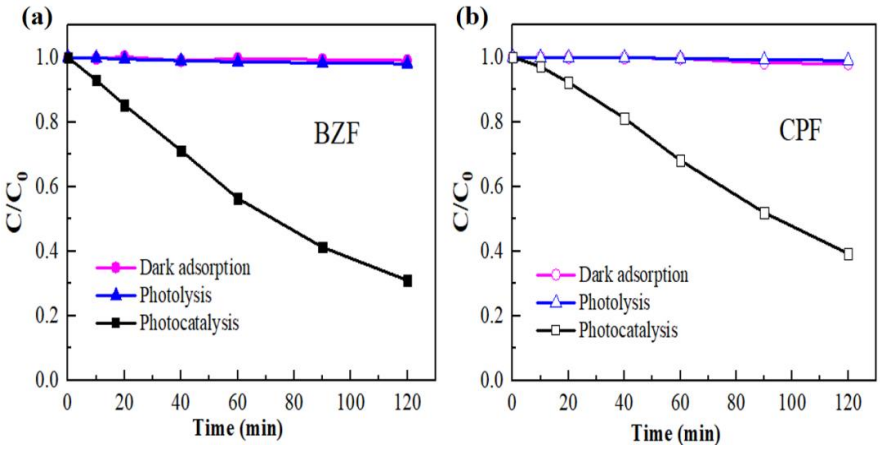


Figure 2. Direct photolysis, dark adsorption, and photocatalytic degradation of (**a**) BZF and (**b**) CPF (C_0 = 1 mg/L).

From Figure 2, it can be seen that 69.0% BZF and 60.7% CPF could be removed during 120 min photocatalysis, and their corresponding rate constant k_{20} reached 0.008 min^{-1} and 0.004 min^{-1}, respectively. This indicates the effective photocatalytic performance of the NF-TNAs. Notably, the degradation efficiency of BZF was slightly higher than that of CPF. This can be attributed to the existence of Cl substituent on CPF, leading to the enhancement of an electron-withdrawing effect on this site. As the ROS mainly attacked the benzene ring of fibrates, the reaction between the benzene ring and ROS will be weakened and the passivation of CPF is higher than BZF. The stability analysis of the NF-TNAs was conducted by successive tests of BZF degradation, and the results are shown in Figure S3. It is obvious that the degradation efficiency of BZF can be maintained stable at about 69.0% after five cycle tests, which demonstrates that the NF-TNA has high stability under simulated sunlight irradiation.

The effects of BZF/CPF initial concentration on the degradation of BZF/CPF in NF-TNAs/sun system are shown in Figure 3a,b. With the increase in initial BZF/CPF concentration from 0.05 mg/L to 1 mg/L, the degradation rate gradually decreased. One possible reason was that the limited amount of reaction sites on the NF-TNAs could generate the corresponding limited active species during BZF/CPF degradation [37]. Therefore, lower initial concentration of BZF/CPF can be degraded more rapidly. Another reason was that with the increase in BZF/CPF concentration, the charge carriers were more easily adsorbed by BZF/CPF rather than the NF-TNAs surface, leading to the lower activity of the NF-TNAs. Additionally, the enhanced competitive effect for the limited ROS between BZF/CPF molecules and the deuterogenic TPs might partially have adverse effects on BZF/CPF degradation.

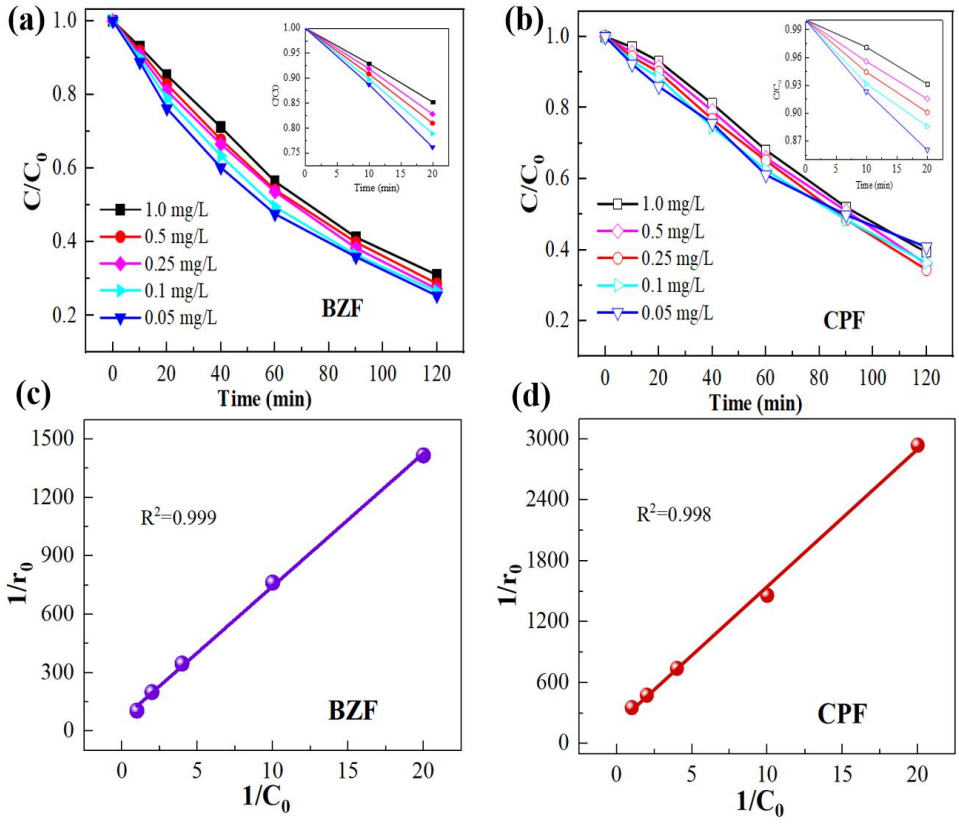


Figure 3. (**a**,**b**) Effects of different initial concentrations on photocatalytic degradation of BZF/CPF, (**c**,**d**) relationship between $1/r_0$ and $1/C_0$.

The photocatalytic oxidation kinetics of diverse organic compounds were evaluated using the Langmuir–Hinshelwood (L–H) model. This rate equation has been widely applied in heterogeneous photocatalysis to establish correlations between degradation rates and organic substrate concentrations [38,39]. The relationship between initial degradation rate and substrate concentration was determined using the Langmuir–Hinshelwood (L–H) pseudo-first-order kinetic model:

$$r_0 = -dC/dt = k_1 \frac{k_2 C_0}{1 + k_2 C_0} \quad (2)$$

which also gives the linear form:

$$\frac{1}{r_0} = \frac{1}{k_1 k_2} \bullet \frac{1}{C_0} + \frac{1}{k_1} \quad (3)$$

In this equation, r_0 represents the fibrate degradation rate (mg/(L·min)), C_0 denotes initial concentration of fibrates, k_1 (mg/(L·min)) is surface reaction kinetic rate constant, and k_2 (L/mg) corresponds to the Langmuir adsorption constant. The L-H kinetic approach has been widely employed in heterogeneous photocatalysis research, which as documented in numerous previous studies. According to Equation (3), the plot of $1/r_0$ versus $1/C_0$ represented in Figure 3c,d shows a linear variation, confirming the applicability of the Langmuir–Hinshelwood model to describe the initial degradation kinetics. The k_1 and k_2 value of BZF calculated from the intercept and the slope of the straight line (R^2 = 0.999) were 0.017 mg/(L·min) and 0.869 L/mg, respectively. The calculated values for k_1 and k_2 of CPF were 0.005 mg/(L·min) and 1.421 L/mg. Therefore, the photocatalytic degradation of BZF/CPF in NF-TNAs/sun satisfactorily follows the Langmuir–Hinshelwood model.

3.3. Insights into Reaction Mechanism

To identify the ROS accounting for BZF/CPF degradation in the NF-TNAs/sun system, chemical quenching experiments were conducted to evaluate the role of hydroxyl radicals (•OH), photo-induced holes (h^+), singlet oxygen ($^1O_2$), and superoxide radicals ($O_2^{\bullet -}$). The results of quenching experiments are shown in Figure 4, and the pseudo-first-order rate constants k_{20} and total degradation efficiencies of BZF/CPF at various situations are summarized in Table 1. Additionally, electron paramagnetic resonance (EPR) spectroscopy was employed to directly confirm the presence of ROS during photocatalytic reaction. DMPO served as a spin-trapping agent to capture $O_2^{\bullet -}$ in methanol solution and •OH in aqueous solution, resulting in the formation of DMPO-$O_2^{\bullet -}$ or DMPO-OH adducts. Additionally, TEMP was applied as spin-trappings to capture $^1O_2$. The EPR spectra are shown in Figure 5a–c.

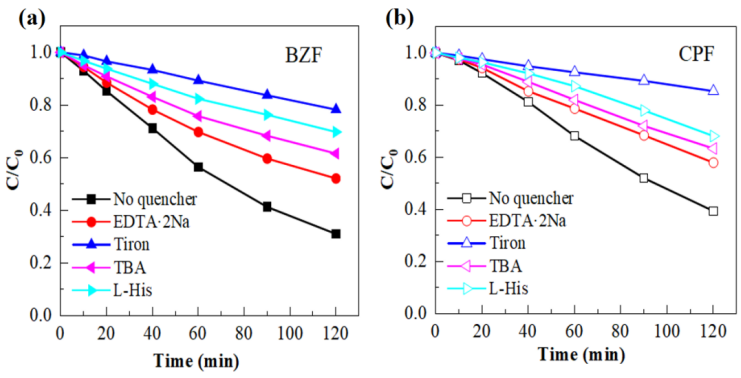


Figure 4. Variation of normalized remaining concentration of (**a**) BZF and (**b**) CPF with time. Influence of different quenchers (C_0 = 1 mg/L).

Table 1. Effects of different quenchers on the kinetics of BZF and CPF degradation (C_0 = 1 mg/L).

Fibrate Drug	Quencher	K_{20} (min^{-1})	K_{120} (min^{-1})	R^2_{120}	Total Removal (120 min)
BZF	Control group	0.008	0.01	0.9982	69.01%
	Tiron	0.0017	0.003	0.9975	21.79%
	TBA	0.0048	0.0041	0.9951	38.47%
	L-His	0.0033	0.003	0.9984	30.26%
	EDTA·2Na	0.0058	0.0055	0.9965	47.93%
CPF	Control group	0.004	0.008	0.9879	60.72%
	Tiron	0.0012	0.0013	0.999	14.68%
	TBA	0.0025	0.0039	0.9934	36.70%
	L-His	0.0023	0.0032	0.9756	31.91%
	EDTA·2Na	0.003	0.0046	0.995	42.15%

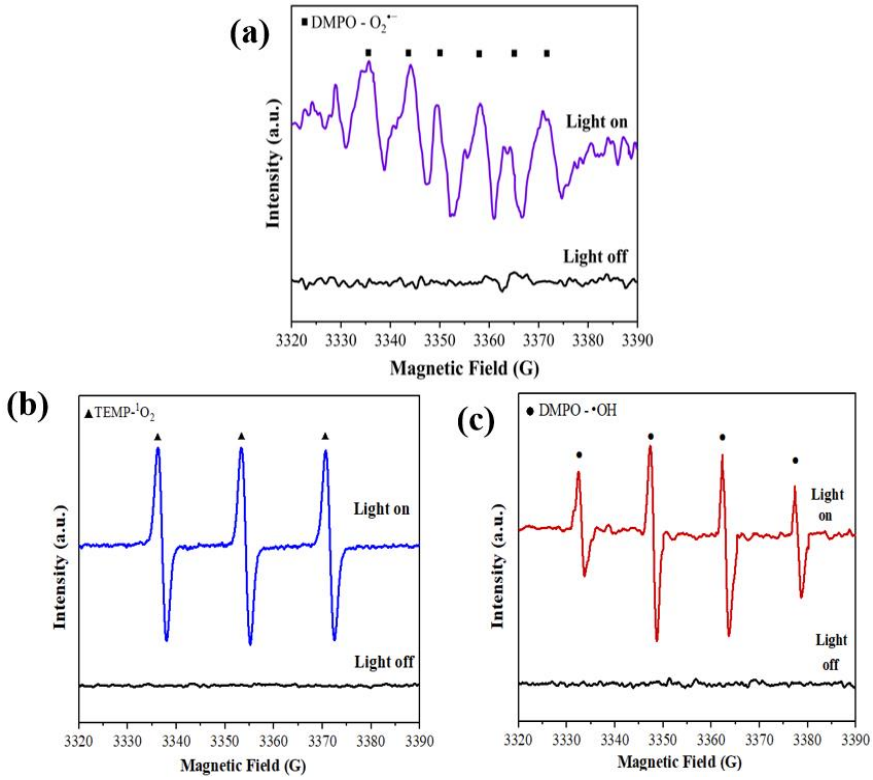


Figure 5. EPR spectra of (**a**) DMPO-$O_2^{\bullet-}$, (**b**) TEMP-$^1O_2$, and (**c**) DMPO-•OH.

As shown in Figure 4 and Table 1, the presence of each quencher reduces BZF/CPF degradation efficiency, confirming the involvement of each ROS in the photocatalytic reaction. For the BZF degradation, k_{20} decreased from 0.0080 min^{-1} to 0.0048 min^{-1} (40.0% reduction), 0.0058 min^{-1} (27.5% reduction), and 0.0017 min^{-1} (78.8% reduction) by, respectively, adding TBA, EDTA·2Na, and tiron. For the CPF degradation, k_{20} decreased from 0.004 min^{-1} to 0.0025 min^{-1} (37.5% reduction), 0.003 min^{-1} (25.0% reduction), and 0.0012 min^{-1} (70.0% reduction) by adding TBA, EDTA·2Na and tiron, respectively. These findings indicate that the contribution of each ROS during BZF/CPF degradation follows the sequence $O_2^{\bullet-}$ > $^1O_2$ >•OH > h^+.

The predominant role of $O_2^{\bullet-}$ played in BZF/CPF degradation can be mainly ascribed to its essential participation in the photocatalytic conversion mechanism. As can be seen in Figure 5a, the typical signal of DMPO-$O_2^{\bullet-}$ adduct with a typical sixfold peak was obviously observed in the EPR spectra of the NF-TNAs/sun system, indicating that $O_2^{\bullet-}$

was generated during photocatalysis. The photo-excited electrons (e^-) from both TiO_2 and pollutant molecules could capture the O_2 molecule to form $O_2^{\bullet-}$ in presence of DO, and this could be the dominant pathway of $O_2^{\bullet-}$ generation in the NF-TNAs/sun system.

In Figure 5b, a signal with a three-line spectrum and relative intensity ratio of 1:1:1 characteristic for TEMP-$^1O_2$ adduct is observed, indicating that a certain amount of $^1O_2$ could also be produced during photocatalysis. It is well known that $^1O_2$ could be produced during $O_2^{\bullet-}$ transformation, and its contribution to fibrate degradation was verified in a previous study [40]. Moreover, the doping of N and F to TiO_2 alters the electronic structure of TiO_2 and favors the single-electron reduction of O_2 to $O_2^{\bullet-}$. Additionally, N and F co-doping makes it possible to extend the lifetime of photogenerated electrons and proves favorable for the separation of h^+ and e^-; thus, more $O_2^{\bullet-}$ can be formed though the reaction between e^- and O_2 [41].

As shown in Figure 5c, the distinctive 1:2:2:1 quartet signal of DMPO-•OH adducts was detected upon exposure to sunlight irradiation, which means that •OH was also generated in the NF-TNAs/sun system. It is well known that the ROS generated throughout photocatalysis can be interpreted by basic reaction Equations (4)–(10). Therefore, it can be also speculated from Equations (7)–(10) that the $O_2^{\bullet-}$ transformation would greatly promote the •OH production [42].

$$h^+ + H_2O \rightarrow \bullet OH + H^+ \quad (4)$$

$$h^+ + OH^- \rightarrow \bullet OH \quad (5)$$

$$e^- + O_2 \rightarrow O_2^{\bullet-} \quad (6)$$

$$e^- + O_2^{\bullet-} + 2H^+ \rightarrow H_2O_2 \quad (7)$$

$$TiO_2(e^-) + H_2O_2 \rightarrow TiO_2 + \bullet OH + OH^- \quad (8)$$

$$O_2^{\bullet-} + H_2O_2 \rightarrow \bullet OH + OH^- + O_2 \quad (9)$$

$$e^- + H_2O_2 \rightarrow \bullet OH + OH^- \quad (10)$$

Although h^+ is considered to be a highly reactive oxidant that can efficiently oxidize surface-adsorbed organics on TNAs, it is difficult to physically transform h^+. Furthermore, previous research indicates that h^+ faces difficulty in oxidizing ambient H_2O to form •OH, as the 2p orbital energy levels of both H_2O and OH^- lie significantly below the valence band edge of TiO_2. Therefore, the contribution of h^+ to BZF and CPF degradation was the lowest. Additionally, the interaction of e^-, O_2, and H^+ can generate hydrogen peroxide (H_2O_2), which subsequently reacts with TiO_2, $O_2^{\bullet-}$, and e^- to produce •OH.

3.4. Possible Degradation Pathways of BZF/CPF During Photocatalysis

The identification of various TPs produced in the degradation of BZF/CPF in the NF-TNA/sun system was performed via LC–MS/MS. As shown in Figure 6, the BZF degradation pathways in the NF-TNA/sun system were proposed based on these identified TPs and analysis of frontier orbital calculation. During photocatalysis, the main ROS for BZF degradation include •OH, $O_2^{\bullet-}$, $^1O_2$, and h^+. In general, the degradation of BZF typically follows three primary pathways. The first pathway is •OH-initiated oxidation of BZF. Hydroxylation was observed to occur on the aromatic ring, as evidenced by the detection of TP1 (m/z = 377) [43–45]. The isosurface of HOMO orbital primarily distributes across the phenoxyaromatic acid fragment of BZF, as presented in Figure S5b, Supplementary Materials. This suggests that this structural fragment will be more vulnerable to being attacked by electrophilic species like •OH, $^1O_2$, and h^+.

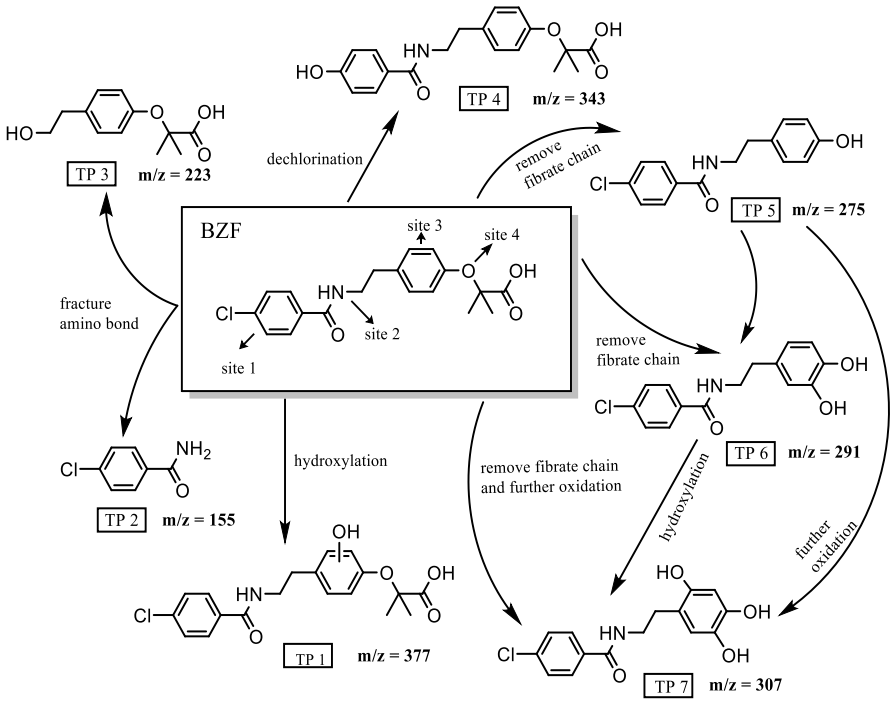


Figure 6. Possible BZF degradation pathways in NF-TNAs/sun system.

The second pathway is the fracture of amino bond. •OH or $O^{\bullet-}$ could attack the amide carbonyl group connected by two benzene rings and will result in TP2 and TP3 generation. As illustrated in Figure S5b, the N9 atom in BZF participates in both HOMO and LUMO orbitals, making this site susceptible to electrophilic and nucleophilic attacks that can lead to cleavage of the amino bond. The third pathway is oxidative dechlorination. The formation of TP4 (m/z = 343) resulted from radical-induced displacement of the chlorine atom at ipso position (C6) in BZF, yielding a phenolic compound. The fourth pathway is fibrate chain substituent (–O–C(CH_3)$_2$COOH). The fibrate chain (–O–C(CH_3)$_2$COOH) was cleaved, with a hydroxyl group replacing the phenoxy moiety to yield TP5. Additionally, the fibrate chain can function as an electron donor, positively influencing the electron density of connected aromatic ring. As a result, C16 exhibits significantly higher HOMO composition and becomes highly vulnerable to multiple electrophilic species. The •OH addition at ipso-aromatic C16 position facilitated ipso-substitution. This could stabilize the carbon-centered radicals and then result in various TPs generation like TP5. TP5 was subsequently oxidized in a continuous process, yielding TP6 and TP7. Aside from •OH-mediated oxidation, TP5, 6, and 7 (as the phenolic intermediates) could also be generated by $^1O_2$-mediated oxidation through the 1,3-addition, 1,4-cycloaddition, and 1,2-cycloaddition pathways [40,46].

For the CPF, five kinds of TPS were identified with LC-MS/MS, and CPF degradation pathways are illustrated in Figure 7. As seen from the frontier orbital location of CPF shown in Figure S6b, both HOMO and LUMO orbitals mainly locate on the cyclopropyl fragment and benzene ring, indicating that both nucleophilic reaction and electrophilic reaction could occur on this position. Notably, the fibrate chain of CPF makes higher contribution to HOMO orbital proportion than that of LUMO orbital, illustrating that electrophilic reaction may more easily occur in this region. The possible degradation pathways of CPF in the NF-TNAs/sun system were also proposed based on these identified TPs and frontier orbital calculation. As the molecular structure of CPF is simpler than BZF, the TP kinds of CPF are less than BZF. Three main degradation pathways are proposed, and the first pathway is •OH-initiated hydroxylation. •OH could attack the phenoxy ring of phenoxyaromatic acid

fragment and lead to the formation of •OH additive products (TP1). Further hydroxylation will produce TP2 and TP5, and TP5 could also be produced by various ROS attacking the cyclopropyl and fibrate chain. The second pathway is that •OH, h^+, or $^1O_2$ could attack the benzene ring and lead to the oxidative cleavage of benzene ring and produce TP3. The third pathway is fibrate chain removal. •OH, h^+, $O_2^{\bullet -}$, and $^1O_2$ attack could cause the fibrate chain loss of CPF, and continuous •OH-initiated hydroxylation will result the production of TP4. Additionally, further oxidation of TP4 could also cause the formation of TP5. Subsequently, some functional groups of CPF are lost during degradation, and the its ring structure could be gradually destroyed and finally oxidized into CO_2, H_2O, etc.

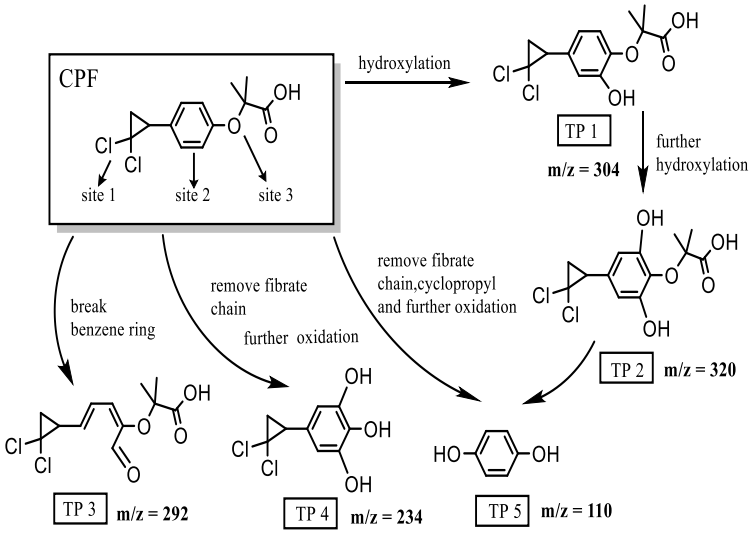


Figure 7. Possible CPF degradation pathways in NF-TNAs/sun system.

3.5. Influence of Environmental Factors and Stability Evaluation

Anions (e.g., Cl^-, $PO^{3-}{}_4$, $CO_3{}^{2-}/HCO_3{}^-$) and natural organic matter (NOM) are widely present in natural aquatic environments, which can affect advanced oxidation processes. The influence of typical anions and NOM during photocatalysis deserves exploration. Therefore, the presence of typical anions ($HCO_3{}^-$, Cl^-, and $PO_4{}^{3-}$) and NOM on BZF/CPF degradation efficiency was studied. Humic acid (HA) was chosen as a representative natural organic matter that exists in almost all the natural water and effluent from wastewater treatment plants at the mg/L concentration level [47]. The results are illustrated in Figure 8.

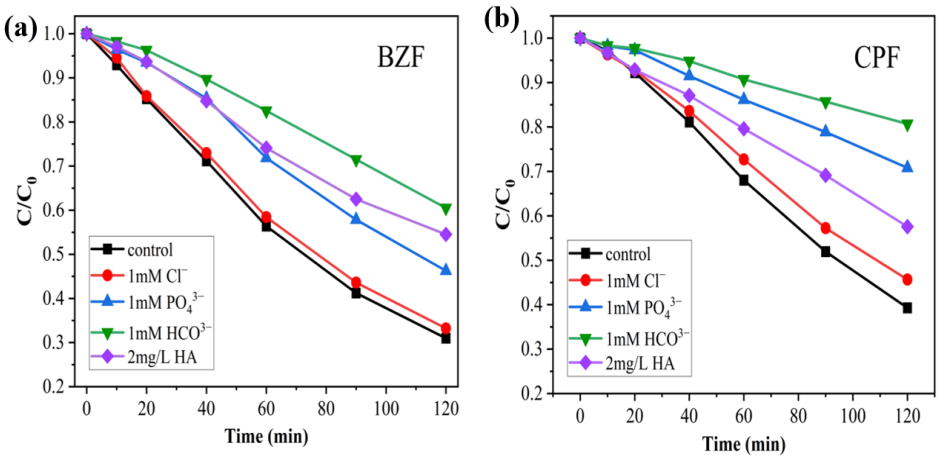


Figure 8. Influence of different anions and humic acid on (**a**) BZF and (**b**) CPF degradation (C_0 = 1 mg/L).

As presented in Figure 8, no apparent decrease was observed as the concentration of Cl^- increased from 0 to 1 mM, meaning that the NF-TNAs/sun system possessed high resistance to Cl^--containing water. Cl^- can react with •OH to produce hypochlorous acid radicals ($ClOH^{\bullet-}$), and $ClOH^{\bullet-}$ can subsequently generate chlorine radicals (Cl•) under acidic conditions, also having high oxidation capacity (E° = 2.432 V vs. SHE) [48,49]. As shown in Figure 8, BZF/CPF degradation efficiency reduced from 69.0% and 60.7% to 51.7% and 26.6% when 1mM PO_4^{3-} was added. This inhibitory effect could be ascribed to the competitive adsorption (between PO_4^{3-} and H_2O) and side reactions (between PO_4^{3-} and free radicals) [50]. The presence of bicarbonate (HCO_3^-) at concentration of 1 mM strongly inhibited BZF/CPF degradation, with behavior that could be attributed to the HCO^{3-} scavenging free radicals to produce low reactivity $CO_3^{\bullet-}$. Meanwhile, HCO_3^- could hinder the adsorption ability of BZF/CPF [51,52]. As seen in Figure 8, HA addition would be unfavorable for BZF/CPF degradation. The degradation efficiency decreased from 69.0% to 45.5% and from 60.7% to 37.1% in presence of 1mM HA. This might also be due to the ability of BZF/CPF adsorbing on the NF-TNAs being affected considerably after HA addition. Generally, anions and NOM in real water have a negative influence on wastewater treatment.

3.6. Toxicity Evaluation

To assess the environmental safety of the photocatalytic degradation of BZF/CPF, the acute toxicity (LD_{50}) and developmental toxicity of both the parent compounds and their transformation products were predicted using quantitative structure–activity relationship (QSAR) modeling, performed with the Toxicity Estimation Software Tool (T.E.S.T., Version 4.2.1). Hierarchical clustering was employed as the predictive approach. Figure 9 shows the toxicity evaluation. As presented in Figure 9a,b, the LD_{50} of BZF/CPF and the most of their TPs were not less than 1000 mg/kg, which were classified as "toxic". However, results in Figure 9a reveal that all the TPs of BZF exhibit higher LD_{50} than BZF, indicating that the acute toxicity of TPs decreased compared to that of BZF. This demonstrates that the acute toxicity of pollutants degraded by the NF-TNA/sun system tended to decrease comprehensively. For the CPF shown in Figure 9b, the acute toxicity of TP1 was lower than CPF, while TP2 and TP4 remained at similar acute toxicity to CPF. Notably, the calculated LD_{50} of TP3 and TP5 was greater than 1000 mg/kg, which means that they were "more toxic". Overall, the acute toxicity of pollutants decreases after photocatalysis, while few TPs are more toxic than parent compounds.

Figure 9c,d illustrates the developmental toxicity of BZF/CPF and their TPs. For the BZF shown in Figure 9c, the toxicity of TP6 and TP7 decreased compared to that of BZF, whileTP2, TP3, and TP4 remained similar developmental toxicity as BZF. Additionally, TP1 and TP5 converted into "developmental non-toxicant", which means that they have few toxicities. Additionally, Figure 9d demonstrates that all the developmental toxicity of CPF TPs decreased sharply after CPF degradation. In particular, TP1 and TP2 emerged as "developmental non-toxicant". Based on the toxicity calculation, the proposed NF-TNA/sun system can alleviate the toxicity of BZF/CPF to a great extent.

Based on the toxicity calculation, the NF-TNAs/sun system is able to reduce the BZF/CPF toxicity, but a small number of TPs retain toxic properties. The Microtox® method has been commonly employed to more effectively demonstrate the toxic transformation of fibrates during the AOPs process [53]. This method aims to identify the acute toxicity of pollutants by measuring the luminescence inhibition rate of the treated solution to *V. fischeri*. Therefore, Microtox tests were performed during BZF/CPF degradation, and the results are shown in Figure S9, Supplementary Materials. As can be seen, the luminescence inhibition increased obviously to 63% and 52% in the first 90 min, which could be ascribed to the

formation and accumulation of toxic TPs. However, as the reaction time extended beyond 90 min up to 200 min, a progressive decline in luminescence inhibition was observed from 63% to 15% for BZF and from 52% to 6% for CPF, respectively. This result illustrated that a major quantity of toxic TPs will undergo further degradation or conversion into less toxic derivatives with progressive reaction. Accordingly, as the reaction time increased, these more toxic TPs could be finally degraded or transformed.

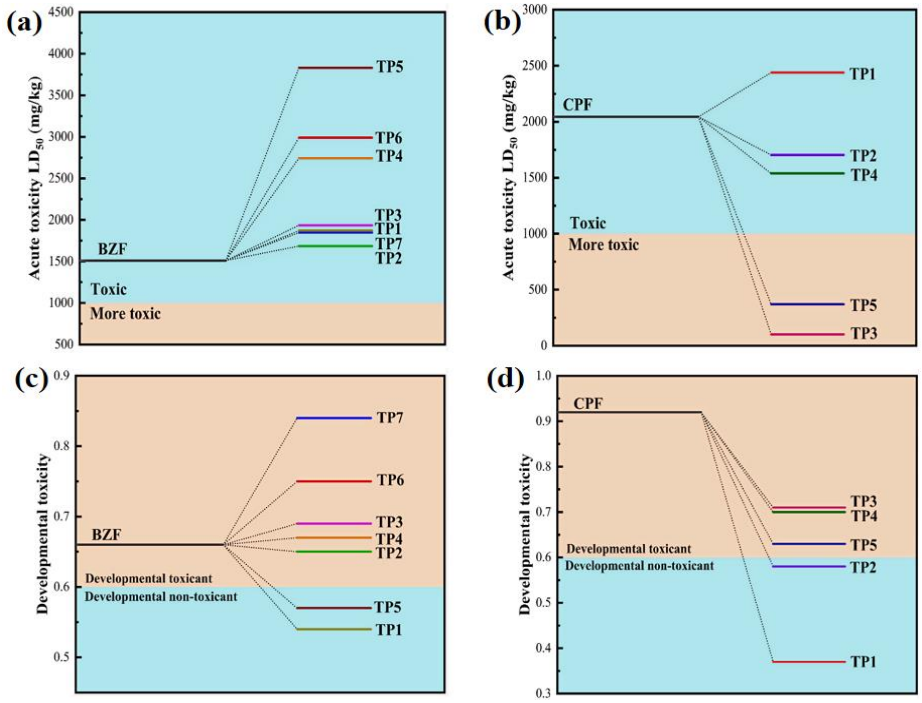


Figure 9. (**a**,**b**) Acute toxicity and (**c**,**d**) developmental toxicity of BZF/CPF TPs in NF-TNAs/sun system.

4. Conclusions

This study demonstrated that BZF and CPF as two representative fibrates, which are resistant to both biodegradation and direct photolysis, can be effectively degraded in water using the NF-TNAs/sun photocatalytic system. The reaction mechanism was determined by employing different quenchers, with experimental results demonstrating that $O_2^{\bullet-}$ and $^1O_2$ were the primary reaction active species. Three inferred BZF degradation pathways including •OH-addition, amino bond fracture, and oxidation dechlorination were proposed based on LC-MS/MS analysis. Additionally, the main CPF degradation pathways were proposed, including •OH initiated hydroxylation, benzene ring cleavage, and fibrate chain removal.

The potential toxicity of BZF/CPF and their transformation products was also predicted, and analysis revealed that certain BZF/CPF TPs exhibited concerning toxicity levels, but prolonged exposure in the NF-TNAs/sun system effectively degraded these compounds through complete mineralization. Research was also conducted to evaluate the impact of different anions and typical NOM on BZF/CPF degradation rates in an NF-TNAs/sun system. The results illustrate that both the anions and humic acid inhibited the degradation of BZF/CPF, but the system was robust. In general, this entire work developed a robust NF-TNAs/sun system for reliable and efficient degradation of typical fibrates, with full investigation of the fibrate oxidation mechanism and degradation pathway. The findings demonstrate not only the effectiveness of NF-TNAs-based photocatalysis for fibrate degradation but also suggest its promising application for treating diverse water contaminants. The methodology developed in this study could be extended to degrade

other classes of pharmaceutical compounds in wastewater, potentially offering a versatile solution for emerging contaminant removal.

Supplementary Materials: The following supporting information can be downloaded at: https://www.mdpi.com/article/10.3390/w17152261/s1, Text S1. The details of the ROS quenching experiments. Text S2. BZF/CPF analysis and identification of transformation products (TPs). Text S3. EPR tests. Figure S1. XRD patterns of the NF-TNAs. Figure S2. The full XPS spectrum of NF-TNAs. Figure S3. UV-vis absorption spectra of BZF and CPF. Figure S4. Cycling tests of NF-TNAs/sun system (Conditions: $[BZF]_0$ = 1 mg/L). Figure S5. (a) Atomic numbering of BZF model (b) Isosurfaces and orbital energies of HOMO and LUMO orbital of BZF. Figure S6. (a) Atomic numbering of CPF model (b) Isosurfaces and orbital energies of HOMO and LUMO orbital of CPF. Figure S7. Total ion chromatogram of BZF by LC-MS/MS. Figure S8. Total ion chromatogram of CPF by LC-MS/MS. Figure S9. Evolution of luminescence inhibition vs reaction time after 10 min of exposure to *V. fischeri* bacteria.

Author Contributions: Methodology, X.C. and J.Y.; Formal analysis, J.G. and T.Z.; Investigation, H.Z.; Data curation, J.G.; Writing—original draft, H.Z.; Writing—review & editing, X.C., J.G. and H.C.; Funding acquisition, X.C., J.Y. and H.C. All authors have read and agreed to the published version of the manuscript.

Funding: This study was financially supported by the National Key Research and Development Program of China (No. 2022YFC3203604); Water Environmental Protection Engineering Research Center of Jiangsu Province, China (2025No. W2502); Technology Innovation and Application Development Project of Chongqing Municipality, China (No. CSTB2022TIAD-GPX0035); and Research on Benefit Evaluation and Policy Suggestions for Recycled Water Utilization of Chongqing, China (No. CQSLK-2022017).

Data Availability Statement: The original contributions presented in this study are included in the article/Supplementary Material. Further inquiries can be directed to the corresponding author.

Conflicts of Interest: The authors declare no conflict of interest.

References

1. Tete, V.S.; Nyoni, H.; Mamba, B.B.; Msagati, T.A.M. Occurrence and spatial distribution of statins, fibrates and their metabolites in aquatic environments. *Arab. J. Chem.* **2020**, *13*, 4358–4373. [CrossRef]
2. Giebultowicz, J.; Stankiewicz, A.; Wroczynski, P.; Nalecz-Jawecki, G. Occurrence of cardiovascular drugs in the sewage-impacted Vistula River and in tap water in the Warsaw region (Poland). *Environ. Sci. Pollut. Res. Int.* **2016**, *23*, 24337–24349. [CrossRef] [PubMed]
3. Kosma, C.I.; Lambropoulou, D.A.; Albanis, T.A. Occurrence and removal of PPCPs in municipal and hospital wastewaters in Greece. *J. Hazard. Mater.* **2010**, *179*, 804–817. [CrossRef] [PubMed]
4. Ido, A.; Hiromori, Y.H.; Meng, L.P.; Usuda, H.; Nagase, H.; Yang, M.; Hu, J.Y.; Nakanishi, T.S. Occurrence of fibrates and their metabolites in source and drinking water in Shanghai and Zhejiang, China. *Sci. Rep.* **2017**, *7*, 45931. [CrossRef]
5. Gworek, B.; Kijeńska, M.; Zaborowska, M.; Wrzosek, J.; Tokarz, L.; Chmielewski, J. Occurrence of pharmaceuticals in aquatic environment—A review. *Desalination Water Treat.* **2020**, *184*, 375–387. [CrossRef]
6. Oliveira, M.A.d.; Silva, G.D.d.; Campos, M.S.T. Chemical degradation kinetics of fibrates: Bezafibrate, ciprofibrate and fenofibrate. *Braz. J. Pharm. Sci.* **2016**, *52*, 545–553. [CrossRef]
7. Wang, J.; Wang, S. Removal of pharmaceuticals and personal care products (PPCPs) from wastewater: A review. *J. Environ. Manag.* **2016**, *182*, 620–640. [CrossRef]
8. Maldonado-Torres, S.; Gurung, R.; Rijal, H.; Chan, A.; Acharya, S.; Rogelj, S.; Piyasena, M.; Rubasinghege, G. Fate, Transformation, and Toxicological Impacts of Pharmaceutical and Personal Care Products in Surface Waters. *Environ. Health Insights* **2018**, *12*, 117863021879583. [CrossRef]
9. Lee, D.-E.; Khan, A.; Husain, A.; Anwar, K.; Lee, H.-C.; Shin, S.-H.; Lee, J.-Y.; Danish, M.; Jo, W.-K. Synergistic performance of Z-scheme based g-CN/$Zn_{0.5}Cd_{0.5}S$/GO nanocomposite towards sustainable model organic pollutants detoxification: Mechanistic insights and practical implications. *J. Alloys Compd.* **2025**, *1022*, 179820. [CrossRef]
10. Liang, X.; Yu, S.; Meng, B.; Wang, X.; Yang, C.; Shi, C.; Ding, J. Advanced TiO_2-Based Photoelectrocatalysis: Material Modifications, Charge Dynamics, and Environmental–Energy Applications. *Catalysts* **2025**, *15*, 542. [CrossRef]

11. Chen, D.; Cheng, Y.; Zhou, N.; Chen, P.; Wang, Y.; Li, K.; Huo, S.; Cheng, P.; Peng, P.; Zhang, R.; et al. Photocatalytic degradation of organic pollutants using TiO_2-based photocatalysts: A review. *J. Clean. Prod.* **2020**, *268*, 121725. [CrossRef]
12. Liu, Y.; Dai, X.; Li, J.; Cheng, S.; Zhang, J.; Ma, Y. Recent progress in TiO_2–biochar-based photocatalysts for water contaminants treatment: Strategies to improve photocatalytic performance. *Rsc. Adv.* **2024**, *14*, 478–491. [CrossRef] [PubMed]
13. Ye, Y.; Bruning, H.; Li, X.; Yntema, D.; Rijnaarts, H.H.M. Significant enhancement of micropollutant photocatalytic degradation using a TiO_2 nanotube array photoanode based photocatalytic fuel cell. *Chem. Eng. J.* **2018**, *354*, 553–562. [CrossRef]
14. Feng, C.; Raziq, F.; Huang, H.; Wu, Z.P.; Alqahtani, H.S.; Alqahtani, R.; Rahman, M.Z.; Chang, B.; Gascon, J.; Zhang, H. Shining Light on Hydrogen: Solar-Powered Catalysis with Transition Metals. *Adv. Mater.* **2025**, *37*, e2410387. [CrossRef] [PubMed]
15. Sayed, M.; Fu, P.; Shah, L.A.; Khan, H.M.; Nisar, J.; Ismail, M.; Zhang, P. VUV-Photocatalytic Degradation of Bezafibrate by Hydrothermally Synthesized Enhanced {001} Facets TiO_2/Ti Film. *J. Phys. Chem. A* **2016**, *120*, 118–127. [CrossRef]
16. Lambropoulou, D.A.; Hemando, M.D.; Konstantinou, I.K.; Thurman, E.M.; Ferrer, I.; Albanis, T.A.; Fernandez-Alba, A.R. Identification of photocatalytic degradation products of bezafibrate in TiO_2 aqueous suspensions by liquid and gas chromatography. *J. Chromatogr. A* **2008**, *1183*, 38–48. [CrossRef]
17. Mor, G.K.; Varghese, O.K.; Paulose, M.; Shankar, K.; Grimes, C.A. A review on highly ordered, vertically oriented TiO_2 nanotube arrays: Fabrication, material properties, and solar energy applications. *Sol. Energy Mater. Sol. Cells* **2006**, *90*, 2011–2075. [CrossRef]
18. Nakata, K.; Fujishima, A. TiO_2 photocatalysis: Design and applications. *J. Photochem. Photobiol. C* **2012**, *13*, 169–189. [CrossRef]
19. Yamada, T.; Gao, Y.F.; Nagai, M. Hydrothermal synthesis and evaluation of-visible-light-active photocatalyst of (N, F)-codoped anatase TiO_2 from an F-containing titanium chemical. *J. Ceram. Soc. Jpn.* **2008**, *116*, 614–618. [CrossRef]
20. Zhang, Z.; Cui, Z.; Xu, Y.; Ghazzal, M.N.; Colbeau-Justin, C.; Pan, D.; Wu, W. A Facile Strategy for the Preparation of N-Doped TiO_2 with Oxygen Vacancy via the Annealing Treatment with Urea. *Nanomaterials* **2024**, *14*, 818. [CrossRef]
21. Yadav, V.; Saini, V.K.; Sharma, H. How different dopants leads to difference in photocatalytic activity in doped TiO_2? *Ceram. Int.* **2020**, *46*, 27308–27317. [CrossRef]
22. Li, R.; Li, T.; Zhou, Q. Impact of Titanium Dioxide (TiO_2) Modification on Its Application to Pollution Treatment—A Review. *Catalysts* **2020**, *10*, 804. [CrossRef]
23. Chakraborty, A.K.; Ganguli, S.; Sabur, M.A. Nitrogen doped titanium dioxide (N-TiO_2): Electronic band structure, visible light harvesting and photocatalytic applications. *J. Water Process Eng.* **2023**, *55*, 104183. [CrossRef]
24. Xia, B.; Yao, J.-j.; Han, C.-x.; Zhang, Z.; Chen, X.-y.; Fang, Y.-j. Degradation of ofloxacin by UVA-LED/TiO_2 nanotube arrays photocatalytic fuel cells. *Chem. Pap.* **2017**, *72*, 359–368. [CrossRef]
25. Chen, X.; Yao, J.; Dong, H.; Hong, M.; Gao, N.; Zhang, Z.; Jiang, W. Enhanced bezafibrate degradation and power generation via the simultaneous PMS activation in visible light photocatalytic fuel cell. *Water Res.* **2021**, *207*, 117800. [CrossRef] [PubMed]
26. Rodriguez, E.M.; Marquez, G.; Tena, M.; Alvarez, P.M.; Beltran, F.J. Determination of main species involved in the first steps of TiO_2 photocatalytic degradation of organics with the use of scavengers: The case of ofloxacin. *Appl. Catal. B-Environ.* **2015**, *178*, 44–53. [CrossRef]
27. Chi, Y.; Wang, W.; Zhang, Q.; Yu, H.; Liu, M.; Ni, S.; Gao, B.; Xu, S. Evaluation of practical application potential of a photocatalyst: Ultimate apparent photocatalytic activity. *Chemosphere* **2021**, *285*, 131323. [CrossRef]
28. Lee, D.-E.; Danish, M.; Jo, W.-K. Two in one is really better: NiAl-LDH/[CoNi(μ_3-tp)$_2$(μ_2-py)$_2$] nanocomposite for enhanced antibiotic norfloxacin degradation and H_2 evolution reaction. *Sep. Purif. Technol.* **2024**, *332*, 125748. [CrossRef]
29. Frisch, M.; Trucks, G.; Schlegel, H.; Scuseria, G.; Robb, M.; Cheeseman, J.; Scalmani, G.; Barone, V.; Mennucci, B.; Petersson, G. *Gaussian 09*; Gaussian Inc: Wallingford, CT, USA, 2009.
30. Lu, T.; Chen, F.W. Calculation of Molecular Orbital Composition. *Acta Chim. Sin.* **2011**, *69*, 2393–2406.
31. Kumar, N.; Maitra, U.; Hegde, V.I.; Waghmare, U.V.; Sundaresan, A.; Rao, C.N. Synthesis, characterization, photocatalysis, and varied properties of TiO_2 cosubstituted with nitrogen and fluorine. *Inorg. Chem.* **2013**, *52*, 10512–10519. [CrossRef]
32. Mittal, A.; Mari, B.; Sharma, S.; Kumari, V.; Maken, S.; Kumari, K.; Kumar, N. Non-metal modified TiO_2: A step towards visible light photocatalysis. *J. Mater. Sci.-Mater. El.* **2019**, *30*, 3186–3207. [CrossRef]
33. Wu, G.; Wen, J.; Nigro, S.; Chen, A. One-step synthesis of N- and F-codoped mesoporous TiO_2 photocatalysts with high visible light activity. *Nanotechnology* **2010**, *21*, 85701. [CrossRef] [PubMed]
34. Asahi, R.; Morikawa, T.; Irie, H.; Ohwaki, T. Nitrogen-Doped Titanium Dioxide as Visible-Light-Sensitive Photocatalyst: Designs, Developments, and Prospects. *Chem. Rev.* **2014**, *114*, 9824–9852. [CrossRef] [PubMed]
35. Hua, Z.L.; Dai, Z.Y.; Bai, X.; Ye, Z.F.; Gu, H.X.; Huang, X. A facile one-step electrochemical strategy of doping iron, nitrogen, and fluorine into titania nanotube arrays with enhanced visible light photoactivity. *J. Hazard. Mater.* **2015**, *293*, 112–121. [CrossRef]
36. Li, Q.; Shang, J.K. Self-organized nitrogen and fluorine co-doped titanium oxide nanotube arrays with enhanced visible light photocatalytic performance. *Environ. Sci. Technol.* **2009**, *43*, 8923–8929. [CrossRef]
37. Orge, C.A.; Fernando, R.; Pereira, M.; Faria, J.L. Bezafibrate removal by coupling ozonation and photocatalysis: Effect of experimental conditions. *Environ. Nanotechnol. Monit. Manag.* **2022**, *17*, 100610. [CrossRef]

38. Vasanthkumar, K.; Porkodi, K.; Selvaganapathi, A. Constrain in solving Langmuir–Hinshelwood kinetic expression for the photocatalytic degradation of Auramine O aqueous solutions by ZnO catalyst. *Dye. Pigment.* **2007**, *75*, 246–249. [CrossRef]
39. Khezrianjoo, S. Photodestruction of Direct Yellow 11 in aqueous TiO_2 suspension: Effect of operational parameters on detoxification, Langmuir–Hinshelwood kinetic expression and biodegradability. *Desalination Water Treat.* **2019**, *153*, 264–278. [CrossRef]
40. Zhou, Y.; Zhao, J.; Zhang, Y.N.; Qu, J.; Li, C.; Qin, W.; Zhao, Y.; Chen, J.; Peijnenburg, W. Trace amounts of fenofibrate acid sensitize the photodegradation of bezafibrate in effluents: Mechanisms, degradation pathways, and toxicity evaluation. *Chemosphere* **2019**, *235*, 900–907. [CrossRef]
41. Ge, M.Z.; Cao, C.Y.; Huang, J.Y.; Li, S.H.; Zhang, S.N.; Deng, S.; Li, Q.S.; Zhang, K.Q.; Lai, Y.K. Synthesis, modification, and photo/photoelectrocatalytic degradation applications of TiO_2 nanotube arrays: A review. *Nanotechnol. Rev.* **2016**, *5*, 75–112. [CrossRef]
42. Schneider, J.; Matsuoka, M.; Takeuchi, M.; Zhang, J.; Horiuchi, Y.; Anpo, M.; Bahnemann, D.W. Understanding TiO_2 photocatalysis: Mechanisms and materials. *Chem. Rev.* **2014**, *114*, 9919–9986. [CrossRef] [PubMed]
43. Razavi, B.; Song, W.; Cooper, W.J.; Greaves, J.; Jeong, J. Free-radical-induced oxidative and reductive degradation of fibrate pharmaceuticals: Kinetic studies and degradation mechanisms. *J. Phys. Chem. A* **2009**, *113*, 1287–1294. [CrossRef] [PubMed]
44. Yin, Z.; Tian, Y.; Gao, P.; Feng, L.; Liu, Y.; Du, Z.; Zhang, L. Photodegradation mechanism and genetic toxicity of bezafibrate by Pd/g-C_3N_4 catalysts under simulated solar light irradiation: The role of active species. *Chem. Eng. J.* **2020**, *379*, 122294. [CrossRef]
45. Solis, R.R.; Rivas, F.J.; Chavez, A.M.; Dionysiou, D.D. Simulated solar photo-assisted decomposition of peroxymonosulfate. Radiation filtering and operational variables influence on the oxidation of aqueous bezafibrate. *Water Res.* **2019**, *162*, 383–393. [CrossRef]
46. Zhang, S.; Chen, J.; Zhao, Q.; Xie, Q.; Wei, X. Unveiling self-sensitized photodegradation pathways by DFT calculations: A case of sunscreen p-aminobenzoic acid. *Chemosphere* **2016**, *163*, 227–233. [CrossRef]
47. Rodrigues, A.; Brito, A.; Janknecht, P.; Proenca, M.F.; Nogueira, R. Quantification of humic acids in surface water: Effects of divalent cations, pH, and filtration. *J. Environ. Monit.* **2009**, *11*, 377–382. [CrossRef]
48. Mostafa, E.; Reinsberg, P.; Garcia-Segura, S.; Baltruschat, H. Chlorine species evolution during electrochlorination on boron-doped diamond anodes: In-situ electrogeneration of Cl_2, Cl_2O and ClO_2. *Electrochim. Acta* **2018**, *281*, 831–840. [CrossRef]
49. Buxton, G.V.; Greenstock, C.L.; Helman, W.P.; Ross, A.B. Critical Review of rate constants for reactions of hydrated electrons, hydrogen atoms and hydroxyl radicals (OH/O− in Aqueous Solution. *J. Phys. Chem. Ref. Data* **1988**, *17*, 513–886. [CrossRef]
50. Mártire, D.O.; Gonzalez, M.C. Aqueous Phase Kinetic Studies Involving Intermediates of Environmental Interest: Phosphate Radicals and Their Reactions with Substituted Benzenes. *Prog. React. Kinet. Mech.* **2001**, *26*, 201–218. [CrossRef]
51. Liu, T.; Yin, K.; Liu, C.; Luo, J.; Crittenden, J.; Zhang, W.; Luo, S.; He, Q.; Deng, Y.; Liu, H.; et al. The role of reactive oxygen species and carbonate radical in oxcarbazepine degradation via UV, UV/H_2O_2: Kinetics, mechanisms and toxicity evaluation. *Water Res.* **2018**, *147*, 204–213. [CrossRef]
52. Kasprzyk-Hordern, B.; Ziolek, M.; Nawrocki, J. Catalytic ozonation and methods of enhancing molecular ozone reactions in water treatment. *Appl. Catal. B-Environ.* **2003**, *46*, 639–669. [CrossRef]
53. Goncalves, A.; Orfao, J.J.M.; Pereira, M.F.R. Ozonation of bezafibrate promoted by carbon materials. *Appl. Catal. B-Environ.* **2013**, *140*, 82–91. [CrossRef]

Disclaimer/Publisher's Note: The statements, opinions and data contained in all publications are solely those of the individual author(s) and contributor(s) and not of MDPI and/or the editor(s). MDPI and/or the editor(s) disclaim responsibility for any injury to people or property resulting from any ideas, methods, instructions or products referred to in the content.